Evaluation of a Thermodynamic Ice Crystal Accretion Model using Experimental Data from NASA's 2nd Fundamental Ice Crystal Icing Test

Ru-Ching Chen*
NASA Glenn Research Center, Cleveland, OH, 44135

Tadas Bartkus† and Jen-Ching Tsao‡
Ohio Aerospace Institute, Cleveland, OH, 44135

Paul von Hardenberg§ and Thomas Ratvasky¶
NASA Glenn Research Center, Cleveland, OH, 44135

A thermodynamic model describing ice crystal icing is evaluated using experimental data collected at NASA Propulsion Systems Laboratory. The model makes the distinction between ice accretions that are "freeze-dominated" and "melt-dominated". Freeze-dominated icing occurs when partially melted ice crystals impact a surface and freeze. This type of icing is characterized by strong adhesion. This contrasts with melt-dominated icing, where un-melted ice crystals adhere to a surface. This type of icing is characterized by weak adhesion. In this paper, the thermodynamic model is used to analyze the ice growth rates and facility conditions to explain possible phenomena such as mass loss as well as the melting and freezing fractions. Previous analyses assumed a collection efficiency of unity at the leading edge of the experimental model. LEWICE is used to determine a better estimate of the collection efficiency at the model leading edge as ice accretion grows in time. The result shows that the sticking efficiency could change in a greater percent with time than previously reported.

I. Nomenclature

CE	=	Collision efficiency for icing probes
$F_{loss,total}$	=	Total mass loss fraction
FR	=	False Response
IWC	=	Ice water content
L_f	=	Latent heat of fusion
LWC	=	Liquid water content
m_0	=	Ice mass melt fraction
$\dot{m}''_{imp,ice}$	=	Mass flux of ice
$\dot{m}''_{imp,liq}$	=	Mass flux of liquid water
$\dot{m}''_{imp,tot}$	=	Total mass flux
MMR	=	Mass mixing ratio
MR	=	Melt ratio
n_0	=	Ice mass freeze fraction
n_{loss}	=	Mass loss due to bounce and erosion
P_0	=	Total pressure
q''_{cond}	=	Conductive heat flux
q''_{conv}	=	Convective heat flux

*Aerospace Engineer, Icing Branch, 21000 Brookpark Road, MS 11-2, AIAA Member.
†Senior Research Associate, Icing Branch, 21000 Brookpark Road, MS 11-2, AIAA Member
‡Principal Research Scientist, Icing Branch, 21000 Brookpark Road, MS 11-2, AIAA Associate Fellow
§Aerospace Engineer, Icing Branch, 21000 Brookpark Road, MS 11-2, AIAA Member.
¶Aerospace Engineer, Icing Branch, 21000 Brookpark Road, MS 11-2, AIAA Senior Member.

q''_{evap}	=	Evaporative heat flux
q''_{freeze}	=	Energy available for freezing
$q''_{kinetic}$	=	Kinetic energy transfer flux
$q''_{sens,ice}$	=	Sensible heat surface energy for ice
$\dot{t}$	=	Leading edge ice growth rate
T_0	=	Total temperature
$\dot{t}_{ND,i}$	=	Non-dimensional growth rate
$T_{RFP,on}$	=	Cloud on rearward facing probe temperature
$T_{RFP,off}$	=	Cloud off rearward facing probe temperature
$T_{PL,on}$	=	Cloud on plenum temperature
$T_{PL,off}$	=	Cloud off plenum temperature
T_{wb0_0}	=	Total wet bulb temperature
TWC	=	Total water content
U	=	Velocity
WE	=	Wire catch efficiency
β	=	Collection efficiency
ρ_{ice}	=	Density of ice
η_{MR}	=	Melt ratio
η_{stick}	=	Sticking efficiency

II. Introduction

ENGINE ice crystal ingestion is of growing concern to jet aircraft. Icing occurs in the compressor region of a jet engine and can lead to jet-engine power-loss events in addition to engine stall, rollback, flameout, and physical damage. These events have been noted to occur at altitudes where water exists in the form of ice crystals. It is postulated by Mason et al. [1] that ice crystals partially melt upon entry into the engine and then accrete on surfaces within the engine core flow path. Researchers have been working to increase understanding the fundamental physics of ice crystal icing. Such research has been conducted at the National Aeronautics and Space Administration (NASA), National Research Council (NRC) of Canada, and the French National Aerospace Center (ONERA), among other institutions.

At NRC Canada, Currie at al conducted a series of ice crystal accretion tests in their Research Altitude Test Facility (RATFac) [2–4]. In these tests, the impact of aerothermal and cloud conditions on the adherence of ice growth was explored. A number of test models including a hemispherical test model was used. In 2013, tests included exploring the effect the ratio of liquid water content (LWC) to total water content (TWC) had on ice growth and accretion adhesion. It was found that this melt ratio is a key factor. In addition, ice accretions reached a steady state size, with an eventual balance between new mass added and erosion. Currie developed a model to describe these observations. This model introduced the concept of sticking efficiency, which is the fraction of impinging water mass flux that is retained on the surface. This model does not take into account heat transfer or phase changes. These experiments revealed there was a maximum sticking efficiency within a set melt ratio range. Outside of the melt ratio range, the sticking efficiency dropped off significantly. This region of higher sticking efficiency is known as an icing severity plateau. Further experiments were conducted at NRC Canada on different geometries and aerothermal conditions [5].

ONERA conducted experiments [6] on a NACA 0012 airfoil as well as a cylindrical airfoil. These experimental results were compared to their numerical icing tool, IGLOO2D [6, 7]. Similar icing plateaus were reported in test results. These tests also modulated the angle of attack and reported lower sticking efficiency at lower angle of attacks. Furthermore, it was also reported that the sticking efficiency decreases with wet-bulb temperature, but is independent of total water content.

A thermodynamic model was developed by Tsao et al. to describe possible icing mechanisms on surfaces within a jet engine [8]. This model predicts that there are two distinct types of conditions which yield ice crystal ice accretions. The first type is a freeze-dominated condition, where partially melted ice crystals accumulate on a surface and freeze. This type of icing is characterized by strong ice accretion adhesion. The second type is melt-dominated, where un-melted ice crystals adhere to a surface. This type of icing is characterized by weak surface adhesion.

In 2016 and 2018, researchers conducted the 2nd Fundamental Ice Crystal Icing Test at NASA Glenn Research Center's Propulsion Systems laboratory [9–14]. Previous papers have compared certain test conditions to the Tsao model. These papers have also added additional heat transfer terms and effects to the model to account for conduction.

Bartkus et al. added a conduction term to account for a temperature difference between the airfoil and impinging ice particles [15]. Later, an additional term was added to account for sub-freezing test model temperatures [13].

This paper examines previously unreported test cases from the 2018 PSL tests and compares those results to the thermodynamic model. The cases attempted to explore the effect of increasing total water content while maintaining constant aero-thermal conditions in the plenum of PSL where water droplets are injected into the flow. However, thermal interaction between the injected water droplets and air resulted in air temperatures and humidity that varied with water content at the downstream test section. This interaction also resulted in a varying degree of water droplet freeze-out, or melt ratio, at the test section. As a result, this paper will compare the accretion growth rate and calculated sticking efficiency for each of the test cases vs. melt ratio. In addition, LEWICE, a numerical ice accretion tool, is used to estimate the collection efficiency, which was previously assumed to be unity for all cases. An evolving convective heat transfer coefficient is also added. These additions attempt to take into account changes due to ice shape growth over time.

III. Thermodynamic Model

A thermodynamic model developed by Tsao et al. was first published in Ref. [8]. Additions to the model are documented by Bartkus et al. in Ref. [13, 15]. These references provide extensive descriptions of the model that will not be repeated in this paper. Instead, a list of model assumptions and a brief overview of the model will be provided below.

The thermodynamic model makes the following assumptions:

- There is steady icing cloud flow and steady air flow relative to the accretion process
- Accretion growth rates apply only to the stagnation point
- Added water mass comes solely from the icing cloud
- Water in the icing cloud is at 0°C

The original model uses an energy balance between the airfoil and the impacting ice crystals. When there is energy available for freezing, the heat flux equation is written as:

$$q''_{freeze} = q''_{evap} - q''_{conv} - q''_{kinetic} - q''_{cond} \tag{1}$$

The heat flux q''_{freeze} will be positive. The evaporative heat transfer flux is denoted q''_{evap}, the convective heat flux transfer flux is denoted q''_{conv}, the kinetic energy transfer flux is denoted $q''_{kinetic}$, and the conductive heat transfer flux is denoted q''_{cond}. The fraction of liquid water that is frozen by q''_{freeze} is n_0, with the two quantities related as

$$q''_{freeze} = \dot{m}''_{imp,liq} \cdot (1 - n_{loss}) \cdot n_0 \cdot L_f \tag{2}$$

where $\dot{m}''_{imp,liq}$ is the mass flux of liquid water, η_{loss} is the fraction of ice mass lost to bounce and erosion, and L_f is the latent heat of fusion. $\dot{m}''_{imp,liq}$ can be expressed in terms of total water content (TWC), melt ratio (η_{MR}), collection efficiency at stagnation line (β_0), and velocity (U). This substitution into Eq. 2 yields

$$q''_{freeze} = (TWC \cdot \eta_{MR}) \cdot \beta_0 \cdot U \cdot (1 - n_{loss}) \cdot n_0 \cdot L_f \tag{3}$$

In the melting-dominated regime, the energy flux balance is:

$$q''_{melt} = q''_{conv} + q''_{kinetic} + q''_{cond} - q''_{evap} \tag{4}$$

The heat flux q''_{melt} will be positive. The fraction of ice that melts is m_0 and is related to q''_{melt} as

$$q''_{melt} = \dot{m}''_{imp,ice} \cdot (1 - n_{loss}) \cdot m_0 \cdot L_f \tag{5}$$

Equation 5 can be also written as

$$q''_{melt} = (TWC \cdot \eta_{MR}) \cdot \beta_0 \cdot U \cdot (1 - n_{loss}) \cdot m_0 \cdot L_f \tag{6}$$

Bartkus et al. [15] evaluated the model with experimental data collected in 2012 at National Research Council (NRC) of Canada's Research Altitude Test Facility (RATFac) and data collected in 2016 at National Aeronautics and Space Administration's (NASA) Propulsion Systems Laboratory (PSL). In this work, a conduction model was also added. The conduction model accommodates the unsteady transfer of heat during a specified initial length of time until the energy flux via conduction reaches 0.

Further experimental comparisons were made by Bartkus et al. [13] with data collected in 2018 in PSL. In addition, the thermodynamic model was modified to accommodate sub-freezing test model temperatures. The new energy flux balance for the freeze-dominated regime is:

$$q''_{sens,ice} + q''_{freeze} = q''_{evap} - q''_{conv} - q''_{kinetic} - q''_{cond} \tag{7}$$

This addition accounts for cooling of the iced surface below freezing by sensible energy, denoted $q''_{sens,ice}$.

The sticking efficiency is a measure of the amount of mass that sticks on a surface to the total amount of mass that impinges on a surface. The sticking efficiency can be calculated in this model as

$$\eta_{stick} = \frac{\dot{t} \cdot \rho_{ice}}{\dot{m}''_{imp,total}} \tag{8}$$

where $\dot{t}$ is the leading edge ice growth rate, and ρ_{ice} is the density of accreted ice. The converse to the sticking efficiency is the fraction of impinging total mass that is lost, known as the mass loss fraction denoted $F_{loss,total}$. The mass loss fraction is calculated as

$$F_{loss,total} = 1 - \eta_{stick} \tag{9}$$

IV. Experimental Description and Data

The data discussed in this paper was collected in 2018 at NASA PSL. Details about the 2018 Second Fundamental Test, including methodology and details on the instruments used to collect thermodynamic data, can be found in Struk et al. [12] as well as Bartkus et al. [13]. For a particular test condition, the total water content, melt ratio, aerothermal data, particle size data, and accretion data were obtained one after another. These measurements could not be taken at the same time as the ice accretion tests since the traversing mechanism for the instruments and accretion airfoil could not be in the test section at the same time. During these runs, intrusive instruments were inserted into the cloud to obtain a measurement. Figure 1 is a diagram of the PSL facility with the traverse systems for the intrusive and non-intrusive probes, as well as the airfoil for accretion testing.

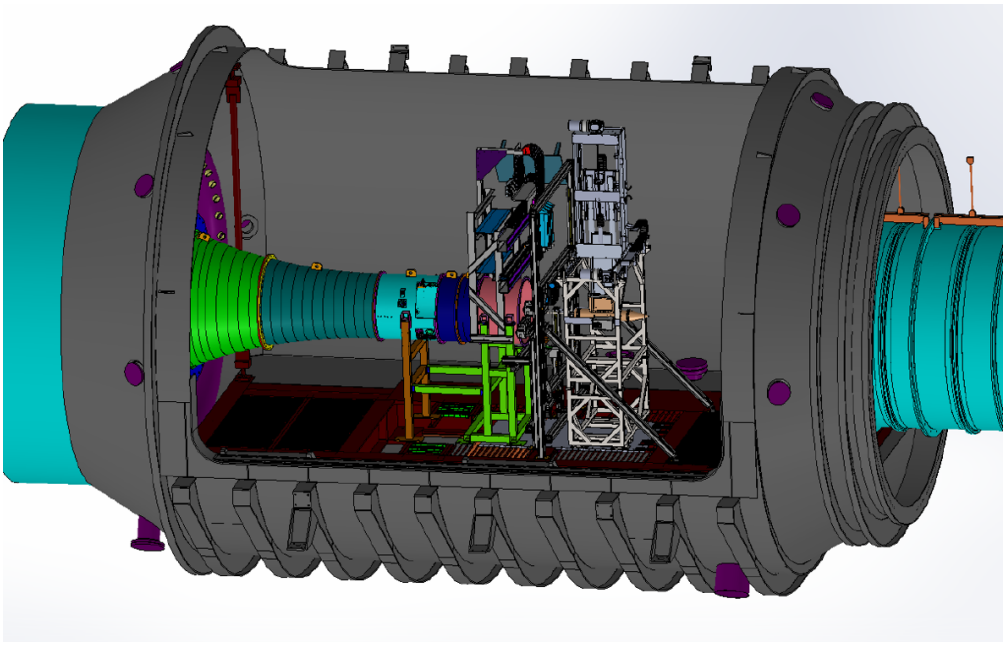

Fig. 1 Solid-Model Image Showing the Traverses for Intrusive Probes, Non-Intrusive Probes, Airfoil/Test Article, and Isokinetic Probe as Installed in PSL.

For the data discussed in the paper, the test conditions are tabulated below in Table 1, alphabetized in increasing order with total water content. The TWC Target is the target bulk value across the test section. There is a duplicate accretion

run for condition B, with the two runs denoted *.a and *.b. These duplicate accretion runs also have corresponding duplicate melt ratio runs that were conducted on the same day. Water content measurements and melt ratio calculations, as well as aerothermal measurements, are discussed below. Note that the total temperature varied between test conditions because of the coupling between the cloud and air temperature. Temperature measurements are described in detail below. Accretion imaging and digitalization is also discussed. Agui et al. and Chen et al. analyzed similar runs total water content sweeps at this test, with some overlap, in Ref. [16] and [17]. In addition, Struk et al. [12] analyzed a relative humidity sweep with test conditions that intersect with the test conditions discussed here.

Table 1 Test conditions (TWC = Total water content, U = Velocity, T_0 = Total temperature, P_0 = Total pressure, MMR = Mass mixing ratio, MR = Melt ratio).

Test Cond.	TWC Target (g/m^3)	TWC IKP (g/m^3)	U (m/s)	T_0 (°C)	P_0 (kPa)	MMR (g/kg)	MR	T_{wb_0} (°C)
A	1	1.25	134	3.0	44.8	6.54	0.23	-1.03
B.a	1.5	2.02	133	2.7	44.7	6.81	0.29	-0.87
B.b	1.5	2.02	132	2.4	44.7	6.81	0.26	-0.96
C	2	3.72	132	2.1	44.7	7.07	0.41	-0.83
D	3.5	5.93	133	1.2	44.8	7.27	0.36	-0.91
E	5	8.06	132	2.5	44.7	7.34	0.51	-0.43

A. Water Content Analysis

Water content measurements were made using the Science Engineering Associates (SEA) Multi-element (MW) probe and the Isokinetic probe (IKP2) at the same location on centerline. These water content measurements were used to calculate the melt ratio, which is the ratio of liquid water content to total water content. Equation 10 describes the calculation of the melt ratio (MR).

$$\text{melt ratio} = \frac{LWC}{TWC} = \frac{LWC}{LWC + IWC} \tag{10}$$

The isokinetic probe was used to make the total water content measurement ($TWC = TWC_{IKP2}$) for the calculation of the melt ratio. Details on the IKP2 calculations, error analysis, and performance testing are described in [18, 19]. The SEA MW uses three heated stainless steel elements to measure liquid water content and total water content. Among these heated elements, there is a 2.1-mm element which was used to obtain a measured liquid water content measurement ($LWC_{2.1}$). This measured water content can be expressed

$$LWC_{2.1} = CE_{2.1}\left(WE_{2.1} \times LWC + FR_{2.1} \times IWC\right) \tag{11}$$

The measured liquid water content value from the probe is assumed to be affected by false response (FR), wire catch efficiency (WE), and collision efficiency (CE). These values can be found in Table 2. Details on this process can be found in Ref. [9]. Note that in order to solve for LWC in Equation 11, ice water content (IWC) must be known. The total water content is the sum of the liquid water content and the ice water content.

$$TWC = LWC + IWC \tag{12}$$

The LWC can then be found by solving Equations 11 and 12 together. Table 2 also contains the average relative humidity levels in the plenum upstream of the spraybars during each of the runs (Accretion RHPL, MW RHPL, IKP RHPL). LWC and TWC measurements, as well as the accretions, were performed during different times using the traverse mechanism. Test operators attempted to maintain steady test conditions in the plenum but there were run to run variations as seen in the RH measurements.

Figure 2 plots the measured total water content, liquid water content, and melt ratio for each of the target total water content values. The measured total water content increases with target total water content, as expected. The target total water content is a bulk average calculated by dividing the injected water mass by a circular area of 24 inches,

Table 2 Test Conditions.

Test Cond.	Accretion RHPL (%)	MW RHPL (%)	IKP RHPL (%)	TWC (g/m^3)	MW 083 (g/m^3)	FR	WE	CE	MR
A	35.2	33.8	34.6	1.25	0.22	0.062	0.591	0.98	0.23
B.a	35.1	34.3	35.4	2.02	0.43	0.065	0.591	0.98	0.29
B.b	35.3	35.3	35.4	2.02	0.40	0.065	0.591	0.98	0.26
C	34.5	34.6	33.8	3.72	1.04	0.068	0.591	0.98	0.41
D	34.9	34.9	34.7	5.93	1.55	0.088	0.591	0.98	0.36
E	35.1	34.9	34.7	8.06	2.72	0.088	0.591	0.98	0.51

which was the assumed cloud diameter. This value does not account for evaporation. The measured value is higher due to the location measured (centerline). This is as observed in Ref. [17]. The melt ratio has a mostly increasing trend, with an exception at Condition C and D (2 and 3.5 g/m^3 target TWC). This is probably an effect from a decrease in total temperature as seen in Table 1. The total temperature for melt-ratio run for Condition D is 1.2°C. This is lower than the other runs, where the temperature was closer to 2.5°C. This lower temperature explains the drop in melt ratio. As previously mentioned, the duplicate accretion run (target water content = 1.5 g/m^3) had its own water content measurements. These points are plotted. The two measured liquid water contents are very similar and are hard to distinguish in Figure 2. However, the difference was large enough to cause a small change in the melt ratio.

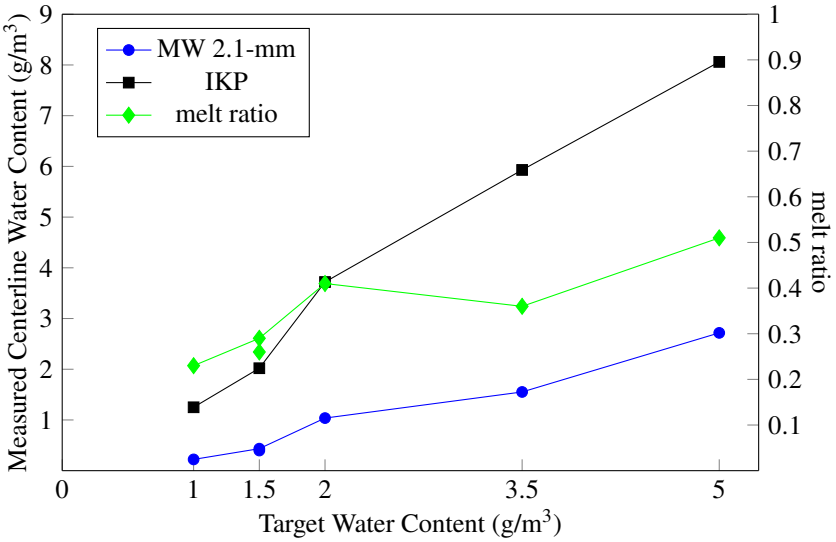

Fig. 2 Target Water Content Plotted Against Measured Water Content.

Note that during the separate runs for each of the instruments, not all aerothermal conditions remained constant. The relative humidity for the accretion runs, multi-wire (melt-ratio) runs, and the isokinetic probe runs are shown in Table 2. Change in relative humidity will have an effect on melt ratio and water content as noted by Struk et al. in Ref. [12]. In the data presented in that reference, changes in the relative humidity between 30% and 40% had greatest impact on the melt ratio. This range corresponds to the Test Conditions investigated in this paper, with a target velocity of 135 m/s and injected water content of 2 g/m^3.

B. Aerothermal Condition Analysis

Measurements of temperature and humidity were estimated using a custom Rearward Facing Probe (RFP) at the test section. More information about the RFP can be found in the literature [10, 14].

Although the total temperature in the plenum was known during the ice accretion tests, it is not representative of the

total temperature at the test section where the ice accretion process occurred. This is due to evaporative cooling that occurs from the introduction of water droplets when the icing cloud is turned on. Furthermore, it was not possible to make direct measurements of the test section temperature during the ice accretion process as the RFP could not be inserted into the airflow at the same time as the airfoil. To estimate the test section temperature of an ice accretion test, a temperature change (ΔT) that represents the change in total temperature at the test section due to evaporative cooling can be determined using RFP measurements taken during separate test runs at the same target conditions as the corresponding ice accretion tests. ΔT can be calculated using

$$\Delta T = \left(T_{RFP,on} - T_{RFP,off}\right) - \left(T_{PL,on} - T_{PL,off}\right) \tag{13}$$

where the first term in parentheses, $T_{RFP,on} - T_{RFP,off}$, is the difference between the cloud-on and cloud-off temperatures as measured by the RFP at the test section. Correction factors were applied to the raw temperature data from the RFP to account for viscous losses that cause the raw temperature measurements to be below that of the true T_0. It can be difficult for the facility to maintain constant conditions throughout a test due to plenum drift, and so some changes in temperature and humidity measured by the RFP cannot be attributed to evaporative cooling effects alone. It is important to isolate the effect of plenum drift from changes due to evaporative cooling which can be done by subtracting the second term in parentheses, $T_{PL,on} - T_{PL,off}$, which is the difference between cloud-on and cloud-off conditions in the plenum. The ΔT value can then be added to the plenum temperature that was measured during the corresponding ice accretion test to approximate what the temperature at the test section was for that test, which are the values in Table 1.

The test section mass mixing ratio (MMR), which is the ratio of water vapor to dry-air mass, is determined in a similar fashion as

$$\Delta MMR = \left(MMR_{RFP,on} - MMR_{RFP,off}\right) - \left(MMR_{PL,on} - MMR_{PL,off}\right) \tag{14}$$

where the first term in the parenthesis, $MMR_{RFP,on} - MMR_{RFP,off}$, is the difference in MMR as measured by the RFP at the test section between cloud on and cloud off conditions while the second term, $MMR_{PL,on} - MMR_{PL,off}$, is the difference in MMR at the plenum between cloud on and cloud off conditions. Like the ΔT value, the ΔMMR value can be added to the plenum MMR that was measured during actual ice accretion test to estimate what the MMR at the test section was that produced the corresponding ice shape.

C. Ice Accretion

The NACA 0012 airfoil was used to collect ice accretions. The airfoil has a chord length of 0.2667 m (10.5 in) and was held at 0° angle of attack. Video recordings of the ice accreting on the airfoil were used to determine the accretion shape as well as the rate of growth over time. Video was captured by two cameras held at orthogonal angles, with one camera capturing a profile view and the other capturing a top-down view (span-wise). Figure 3a shows the profile view of the airfoil during the Test Condition A run after 600 seconds, with the flow direction marked by the black arrows. Figure 3b shows the span-wise (top/down) view at the same time of the Test Condition A test. Only the center 0.127 m (5 in) section of the airfoil, which is made of titanium, is analyzed.

Thermocouples were installed to measure the surface temperature. Temperature data from the runs analyzed are provided in the Appendix.

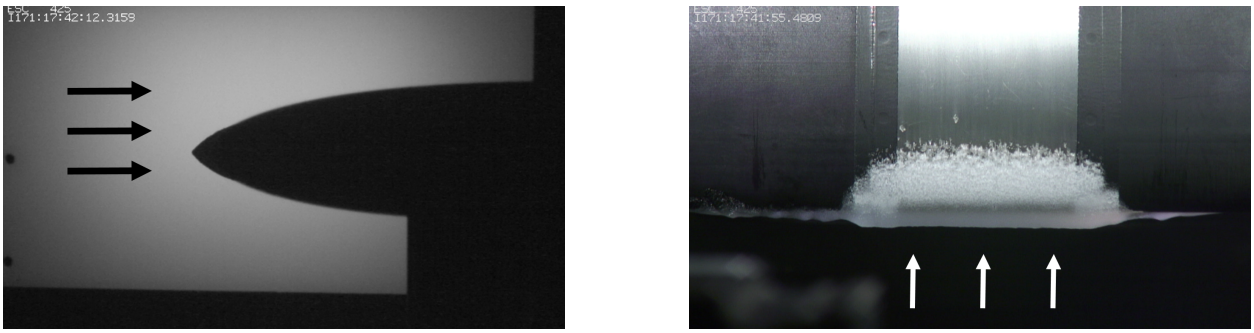

(a) Profile view of accretion **(b) Span-wise view of accretion at center section**

Fig. 3 Video Stills of Accretions from Test Condition A.

The leading edge growth rate measured from the span-view at the mid-span is used for analysis. This is because this camera angle was not hindered by blind spots as the profile view was. The accretion growth rates at discrete time-frames were digitally determined by fitting linear lines to the ice thickness plots (e.g. Figure 4).

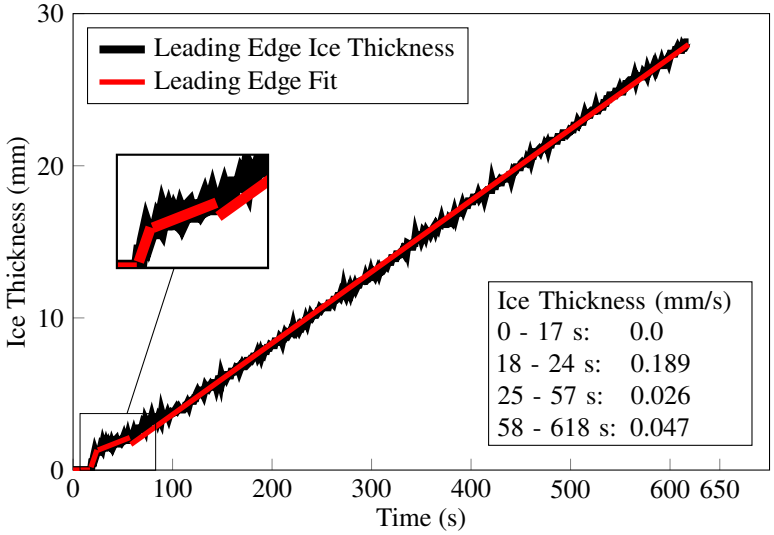

Fig. 4 Ice Thickness of Accretion at Leading Edge During Test Condition B.b.

These accretion growth rates are tabulated in Table 3. The time segments refer to the corresponding growth rates. During the Time 1, there was no accretion. For example, during Condition A, ice growth began by 30 seconds into the accretion run. Time 2 therefore refers to the time when noticeable accretion on the leading edge begins. The ice accretion for Test Condition D shed around 203 seconds. Analysis for this accretion is only conducted to this time. There was no noticeable ice accretion for Test Condition E until 241 seconds.

Table 3 Leading edge ice growth rates at discrete times.

Test Cond.	Growth 1 (mm/s)	Growth 2 (mm/s)	Growth 3 (mm/s)	Growth 4 (mm/s)	Time 1 (s)	Time 2 (s)	Time 3 (s)	Time 4 (s)
A	0	0.026	0.016	0.009	0 - 30	31 - 120	121 - 300	301 - 609
B.a	0	0.094	0.015	0.056	0 - 13	14 - 36	37 - 87	88 - 610
B.b	0	0.189	0.026	0.047	0 - 17	18 - 24	25 - 57	58 - 618
C	0	0.091	0.015	0.081	0 - 19	20 - 35	36 - 307	308 - 636
D	0	0.145	0.035	n/a	0 - 9	10 - 28	29 - 196	Shed Event
E	0	0.014	n/a	n/a	0 - 240	241 - 622	End of Run	

The ice accretion shape was digitalized from the profile view. Optical perspective effects were corrected for. Details on the digitalization and corrections are documented in [20].

The linear growth rate fits can sometimes provide possibly misleading results. In test condition B.b, at time 2, the growth rate is 0.189 mm/s. This value is over double the growth rate in B.a, which is its corresponding repeat run. The time 2 time-span for condition B.b, however, is only 6 seconds compared to the condition B.a time 2 time-span of 22 seconds. The blue fit line in Figure 4 explains why there is this drastic change in growth rate. In all conditions, there was an initial span of rapid growth that slowed with time. The growth rate eventually asymptotically trends towards a fixed growth rate (time 4). As such, the initially high growth rates are not of concern, especially as the rate only existed for a short period of time.

V. LEWICE Analysis

LEWICE (2D, version 3.2.3) was used to determine collection efficiency of the accreted ice shapes [21]. LEWICE was developed by NASA and is a panel-method icing simulation tool which has been validated across a wide range of experimental data. LEWICE is used to calculate the collection efficiency (β or beta) for the clean airfoil, as well as the airfoil after ice has accreted on it. Potential flow codes, such as LEWICE, may not be well-suited for all the geometries from these runs due to separated flow. These results are used to observe whether changes in collection efficiency have an effect on the thermodynamic model results. More accurate collection efficiency calculations should be done in the future.

A. Simulation Set-Up

Facility data from Table 1 were used in conjunction with the digitized experimental profile ice accretions shapes at midspan to run LEWICE. Profile video data only captured the area near the leading edge of the airfoil. As such, the geometry was post-processed to be closed off using generic NACA 0012 airfoil coordinates. Results of this post-processing for test condition C can be seen in Figure 5. Figure 5a shows the clean NACA 0012 airfoil with no visible ice from the profile view. Figure 5b shows the ice shape geometry at 300 seconds in black and the airfoil in red outline. Figure 5c shows the final ice shape at the end of the run.

(a) Cond. C ice shape at 0 s. **(b) Cond. C geometry at 300 s.** **(c) Cond. C geometry at 636 s.**

Fig. 5 Geometry for LEWICE Simulations.

Ice accretion data from Condition E provided ice growth rate, from the span-wise camera, but profile ice shapes at midspan were unobtainable as they were obscured. Figure 6 is a spanwise still from video data taken during the Condition E run. The ice left and right of the midspan is much larger than that at the midspan, making it impossible to identify the ice shape at midspan using the profile view. While test condition E did not provide useful profile view data, the other accretion profile views had no issues.

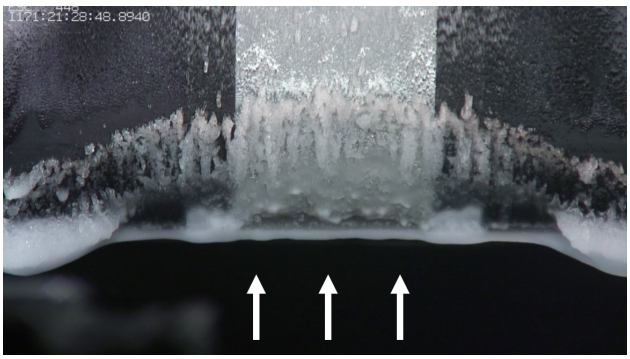

Fig. 6 Ice Thickness of Accretion at Leading Edge During Test Condition E.

Particle size data was collected using the Artium Technologies, Inc Phase Doppler Interferometer (PDI) and a High Speed Imaging (HSI) instrument. For more information on these probes and their use at PSL, refer to [11, 22]. Although full distributions were collected from both instruments, only results calculated from the mean volumetric diameter (MVD) from the PDI are presented. There was negligible difference between the LEWICE collection efficiency results using the MVD and full distributions (less than 1% on a clean airfoil). Table 4 shows the MVD for the conditions collected by the instruments. Both of these instruments were used at the same time during test runs dedicated to measuring particle size. There were two accretion runs associated with Test Condition B (labeled B.a and B.b).

Table 4 Measured Particle Size.

Test Cond.	Target TWC (g/m^3)	IKP TWC (g/m^3)	PDI MVD (μm)	HSI MVD (μm)
A	1	1.25	31.7	33.9
B.a	1.5	2.02	36.9	32.4
B.b	1.5	2.02	36.9	32.4
C	2	3.72	37.2	35.1
D	3.5	5.93	43.3	40.5
E	5	8.06	52.8	46.7

The two instruments follow closely, with the HSI typically measuring lower than PDI, with one exception. As seen in Figure 4, the MVD at Condition C inverts, where the MVD calculated by the PDI is higher than the MVD calculated by the HSI. It is difficult to explain what may have caused this change in trend. It is possible that minerals in the water used during the test may have contaminated the instruments and caused mis-readings. The MVD measured by the PDI was chosen to be used for the LEWICE calculations.

B. Results

A collection efficiency value was calculated at different times during each test using LEWICE. At discrete times, the digitized ice shape geometry was run through LEWICE in conjunction with the measured aerothermal and particle size data. The collection efficiency results for a clean airfoil at each condition is tabulated in Table 5. These values are likely to be more accurate than the collection efficiency results for geometries with ice due to the previously mentioned flow separation issues. Collection efficiencies at different times are plotted in Figure 7. For Condition E, there is no time varying collection efficiency due to videography issues previously mentioned. A few collection efficiencies calculated with both the the HSI and PDI MVDs with a maximum difference is 3%.

Table 5 Collection Efficiency (β) on Clean Airfoil.

Test Cond.	PDI (β)	HSI (β)
A	0.91	0.92
B.a	0.93	0.92
B.b	0.93	0.92
C	0.93	0.92
D	0.94	0.94
E	0.95	0.95

Figure 7 shows the collection efficiency at the leading edge of all the conditions over the length of the run. In general, the collection efficiency decreased, before plateauing. Previously it was mentioned that ice began growing on the leading edge in all conditions after approximately 30 seconds except for Condition E. However, this growth was not always visible from the profile camera and is not shown in Fig. 7. As such, at the first two time-steps for Conditions C and D, there are identical calculated collection efficiencies. The collection efficiency started between 0.91 and just over 0.94 on the clean airfoil and then decreased to around 0.87 to 0.91 as ice accreted. The ice shapes ranged from geometries that were symmetric across the chord to ice shapes that were highly assymetrical. These geoemtries are assumed to cause the decrease in collection efficiency due to the increase in leading edge radius.

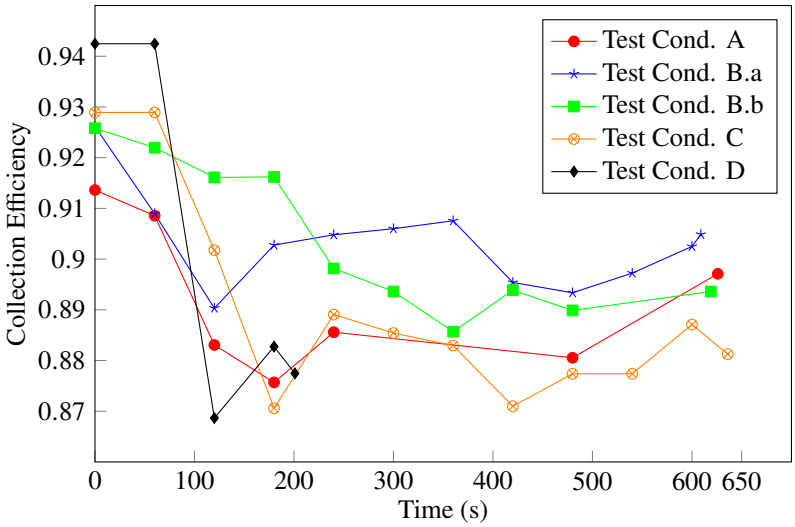

Fig. 7 LEWICE Calculated Collection Efficiency Over Time.

In previous studies by Bartkus et al. [13, 15], the collection was assumed to be 1. Similar studies by Baumert et al. and Currie et. al used steady state ice growth rates. As mentioned above, these collection efficiency values, except for those calculated on a clean airfoil, should not necessarily be assumed to be accurate and are used to observe the effect of non-unity collection efficiencies on the thermodynamic model.

Equation 8 can be rewritten as

$$\eta_{stick} = \frac{\dot{t} \cdot \rho_{ice}}{TWC \cdot \beta_0 \cdot U} \tag{15}$$

where the impinging mass has been written in terms of the total water content, collection efficiency, and velocity. This can further be rearranged as

$$\dot{t}_{ND} = \eta_{stick} \cdot \beta_0 \tag{16}$$

where $\dot{t}_{ND} = \frac{\dot{t} \cdot \rho_{ice}}{TWC \cdot U}$ is defined as the non-dimensional leading edge ice growth rate.

When paired with the collection efficiency results, the non-dimensional leading edge ice growth rate equation can be used to estimate the sticking efficiency. In Table 6, the non-dimensional leading edge growth rate at the beginning ($\dot{t}_{ND,i}$) and end ($\dot{t}_{ND,e}$) of leading edge growth, the corresponding collection efficiencies ($\beta_{0,i}$ and $\beta_{0,e}$, respectively), and sticking efficiency ($\eta_{stick,i}$ and $\eta_{stick,e}$, respectively) are shown for test conditions A, B.a, B.b, and C. Test conditions D and E are not tabulated as test condition D had a shed event, while test condition E did not have two different growth rates.

Table 6 Sticking Efficiency at Beginning and End of Leading Edge Ice Growth.

Test Cond.	$\dot{t}_{ND,i}$	$\beta_{0,i}$	$\eta_{stick,i}$	$\dot{t}_{ND,e}$	$\beta_{0,e}$	$\eta_{stick,e}$
A	0.14	0.91	0.16	0.05	0.90	0.06
B.a	0.32	0.93	0.35	0.19	0.90	0.21
B.b	0.65	0.93	0.70	0.16	0.89	0.18
C	0.17	0.93	0.18	0.15	0.88	0.17

The sticking efficiency changes from the beginning of leading edge accretion to the end of leading edge growth in all cases. In Conditions A, B.a, and B.b, the change is quite noticeable, while there is only a small change in condition C. While these values will propagate any errors in the calculated collection efficiency, the dramatic change between the start and end of growth suggests that the sticking efficiency varies with time. This change may be associated with surface thermal properties. It is noted that the collection efficiency β is a collision efficiency as impinging particles that impact

are not guaranteed to stick. Further investigation and better simulation of the flow field by including viscous effects will provide a more accurate collection efficiency calculation. This will provide more confidence in the calculated sticking efficiency.

VI. Thermodynamic Model Analysis and Discussion

A. Sticking Efficiency

Results are compared at the time when leading edge growth begins and when it ends. This is visualized using growth rates from the span-wise camera view. These times vary between runs, with leading edge growth typically beginning at or before 30 seconds. Test Condition E was the single exception, with leading edge ice growth beginning after 4 minutes. Leading edge ice growth never ended before the end of the test run and, as such, the leading edge ice growth end time is analogous to the end of the test run. This time is between 609 and 622 seconds from the start of the run.

The sticking efficiency was calculated using a collection efficiency of unity as well as a LEWICE calculated collection efficiency. Figure 8 shows the sticking efficiency plotted against melt ratio at the beginning of each test. There was a maximum variation of 9% in the sticking efficiency between calculations using the different collection efficiencies. There is a maximum sticking efficiency at a melt ratio between 0.25 and 0.3. The sticking efficiency decreases with increasing melt ratios and approaches 0. This trend corresponds with the sticking efficiency plateaus described by Currie et al with generally similar maximum sticking efficiencies [2]. These test conditions are similar to TCS-2 as described by Bartkus et al. in [13]. The melt ratios at which the plateau occurs correspond well, although the melt ratio range for the plateau is seemingly narrower than that reported by Bartkus. However, the sparse data presented here make drawing concrete conclusions difficult. The outlier point at an approximate melt ratio of 0.25 is from test condition B.b. As mentioned before, this growth rate only existed for a short period of time (6 seconds).

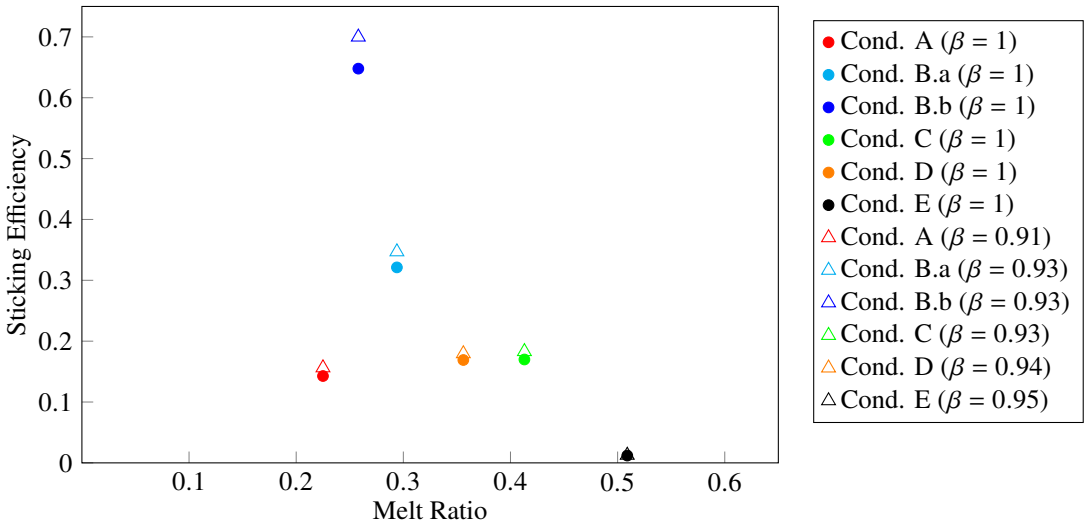

Fig. 8 Sticking Efficiency Plotted Against Melt Ratio at Beginning of Leading Edge Ice Growth.

Figure 9 shows the sticking efficiency plotted against the melt ratio at both the beginning and the end of the accretions. All of these values used LEWICE calculated collection efficiencies. For calculations at the end of the accretion time, the maximum difference between calculations from the collection efficiency of unity and LEWICE values is 12%. There is no data point for Test Condition D at the end of accretion as no ice shape data was collected past 200 seconds due to an ice shed event.

The sticking efficiency again has a plateau between a melt ratio of approximately 0.25 to 0.3 for the limited number of data points. Test Condition B.b, which has the high sticking efficiency at the start of growth, has a much lower sticking efficiency at the end of growth period. The sticking efficiency at the end of growth between the repeated Test Condition B run yield only slightly different values, with the higher melt ratio case yielding a higher sticking efficiency. The sticking efficiency at higher melt-ratio conditions do not change much in value during the run as seen with Test Conditions C and E.

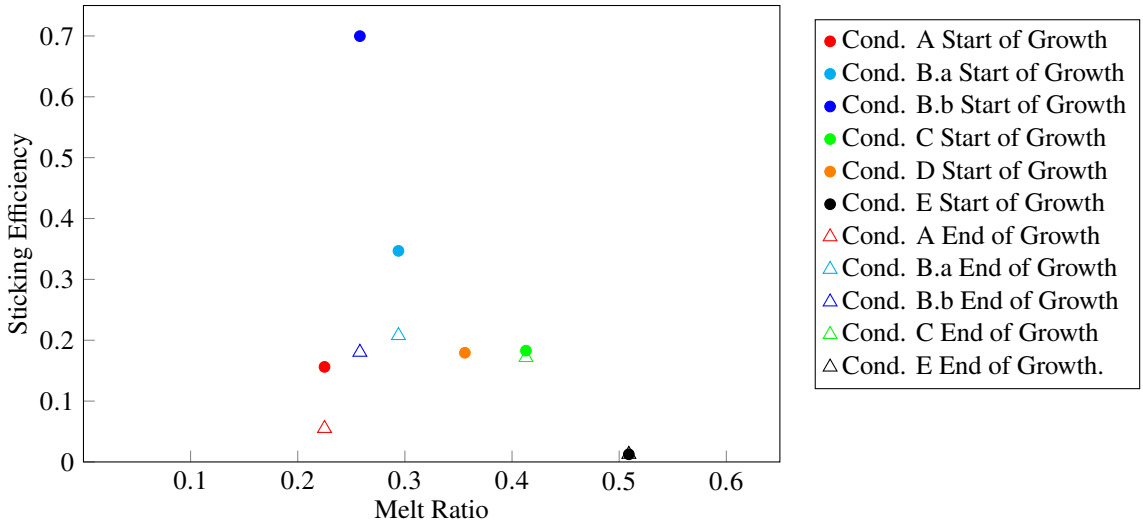

Fig. 9 Sticking Efficiency vs Melt Ratio

Overall, the melt ratio at which the sticking efficiency plateau occurs is much narrower and on the low end of that reported by Baumert et al [6], but higher than that reported by Currie et al. [3]. Baumert reported the sticking efficiency plateau occurring between melt ratios of 0.2 and 0.6. Here, the reported sticking efficiencies at the plateau during the beginning of the run are in the range of 0.3 to 0.7. However, at the end of accretion, the sticking efficiencies reported here are lower, with the plateau occurring around a sticking efficiency of 0.2. This corresponds with previously reported data by Bartkus et al. [13] which utilized data from the same test campaign. The tests conducted by Baumert were conducted at lower speeds (40 m/s), lower total wet bulb temperatures (-15°C and -5°C), and higher MVD (80 μm). These differences may account for the difference in plateau characteristics.

Currie et al. [3] reported the sticking efficiency plateau occurring between melt ratios of 0.1 and 0.25, which is lower than what is reported here, although there is no data at lower melt ratios in this set of analyzed accretion runs. The sticking efficiency at the plateau was reported to be between 0.27 and 0.4. Again, this corresponds well with the sticking efficiency reported here at the beginning of accretion (with the exception of outlier point at Test Condition B.b), but not at the end. In 2014, the sticking efficiency plateau was reported at approximately the same range of melt ratios, although higher sticking efficiencies were reported. These tests were conducted at Mach 0.25 and 0.4 (the higher of which corresponds with the test conditions of data reported here), with a higher MVD (57μm), and warmer temperatures (0°C to 6°C).

B. Mass Loss Fraction

Figure 10 plots the mass loss fraction against melt ratio at the start and end of leading edge ice growth. The mass loss fraction is calculated using Equation 9. The red markers are total mass loss fraction at the start of leading ice growth, while the blue markers are total mass loss fraction at the end of leading edge ice growth. There is a decrease in total mass loss between melt ratios of 0.25 and 0.3, which correlates with the plateau seen in Figure 9. As more particles are sticking to the surface, there is less mass loss. The mass loss associated with splash and runback (not shown here) increases with melt ratio due to more liquid water content. These results correlate well with those presented by Bartkus et al. [13].

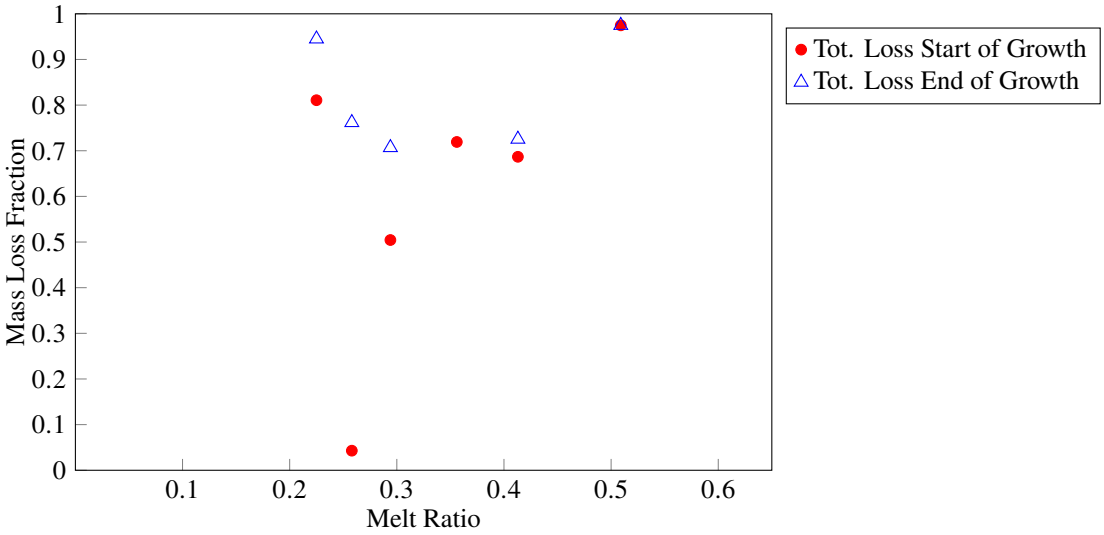

Fig. 10 Total (tot.) Mass Loss Fraction Plotted Against Melt Ratio.

The total mass loss increases from the beginning of growth to the end of growth. This corresponds with the decrease in growth rate from the beginning to the end of growth. The dip in mass loss fraction may span a wider melt ratio range at the end of growth compared with the beginning of growth.

C. Freeze and Melt Fraction

Figure 11 shows the freeze and melt fractions at different total wet bulb temperatures and the start and end of leading edge ice growth. The freeze and melt fractions can be found be solving Equations 3 and 6, respectively, and depends on whether there is energy available for freezing or melting. All plotted values are calculated using LEWICE calculated collection efficiencies. Bartkus et al. [13] noted that there is a transition between melt-dominated and freeze-dominated icing around −0.5°C and −1.0°C. Here, the transition region appears to be around −0.9°C and −1.0°C, although the limited data set hinders this accuracy. The transition occurs below 0°C due to kinetic energy of the impinging cloud. All melt and freeze fractions above approximately −0.9°C are quite small and are within error of being either slightly freezing or slightly melting, which explains the one outlier freeze point at around −0.4°C.

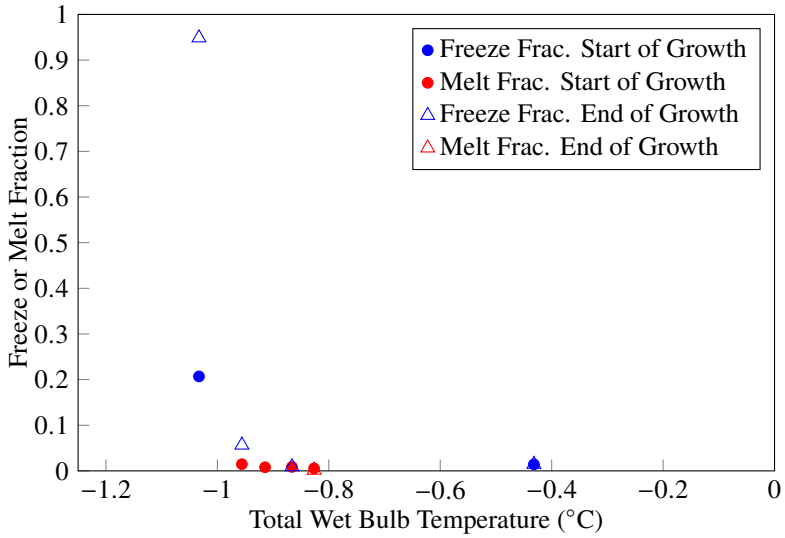

Fig. 11 Freeze or Melt Fraction vs Total Wet Bulb Temperature

The values plotted in Figure 11 are presented in Table 7 where the subscript i refers to the beginning of leading edge ice growth and the subscript e refers to the end of leading edge ice growth. As mentioned before, at total wet bulb temperatures approximately −0.9°C and under, the melt and freeze fractions are very small and are within error of switching to freeze or melt conditions, respectively.

Table 7 Melt (m_0) and Freeze (n_0) Fraction at Start and End of Leading Edge Growth

0	$n_{0,i}$	$m_{0,i}$	$n_{0,e}$	$m_{0,e}$
−0.43	0.014	-	0.014	-
−0.83	-	0.005	-	0.001
−0.87	-	0.009	0.009	-
−0.91	-	0.008	-	-
−0.96	-	0.015	0.057	-
−1.03	0.207	-	0.949	-

VII. Conclusion

This paper presents the accretion growth rate and calculated sticking efficiency for ice-crystal icing experiments where the melt ratio of the impinging cloud is varying. The results are further compared to a thermodynamic model which assesses the local energy balance for freeze or melt dominated conditions. Different from previous work, the model uses non-unity collection efficiency values calculated using LEWICE. Consistent with similar experiments, the wet bulb temperature was observed to be an important factor in determining the type of icing that will accrete. A transition to freeze-dominated conditions was calculated to occur using the thermodynamic model when the air wet-bulb temperature was below approximately -1ïĆřC. The sticking efficiency versus melt ratio of the impinging ice cloud had a plateau region which corresponds well with other data analyzed from the same test campaign. While the sticking efficiencies in the plateau from previously analyzed data were lower than results reported by Currie et al. [3], results presented here do compare well with CurrieâĂŹs results, where they reported a sticking efficiency plateau between 0.27 to 0.4 at melt ratios between 0.1 and 0.25. For the data analyzed in this paper, the sticking efficiencies in the plateau ranged from 0.2 to 0.7 (including data from both the start and end of ice growth) at melt ratios between 0.25 and 0.3. This plateau spans a slightly lower melt ratio range compared to previously presented results from the same test campaign. LEWICE results show that the collection efficiency of the cloud changes over time due to the evolving ice shape. This, together with changing surface properties such as temperature, result in a calculated sticking efficiency that changes in time, which is not currently captured in the thermodynamic model. Further work will be required to better characterize sticking efficiency and what factors drive its change over time.

Appendix

Thermocouple TC03 is located at the leading edge along the centerline of the airfoil. TC06, TC10, TC13, and TC14 are located progressively further downstream of the airfoil along the centerline. See [13] and [12] for more information on thermocouple locations.

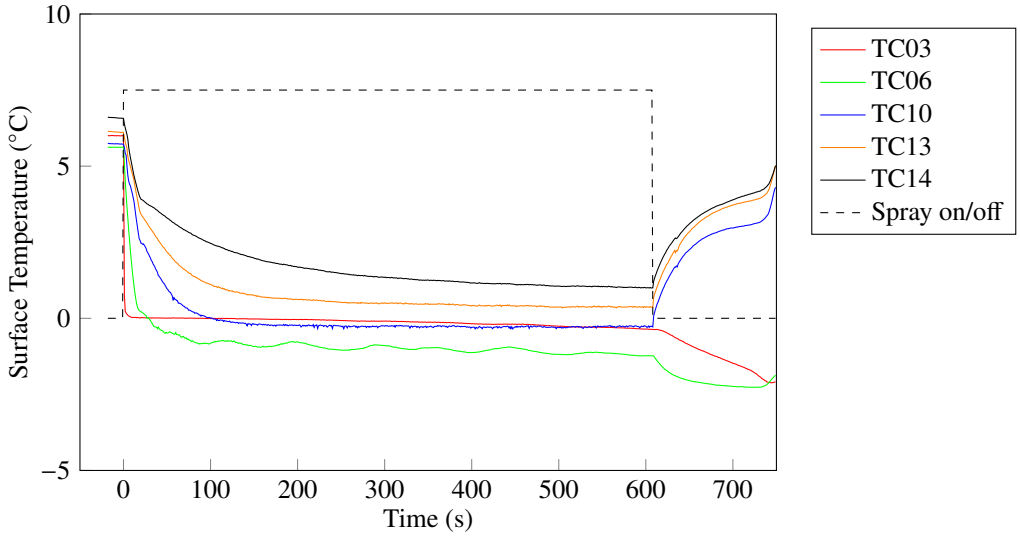

Fig. A.1 Airfoil Surface Temperatures Over Time during Test Condition A.

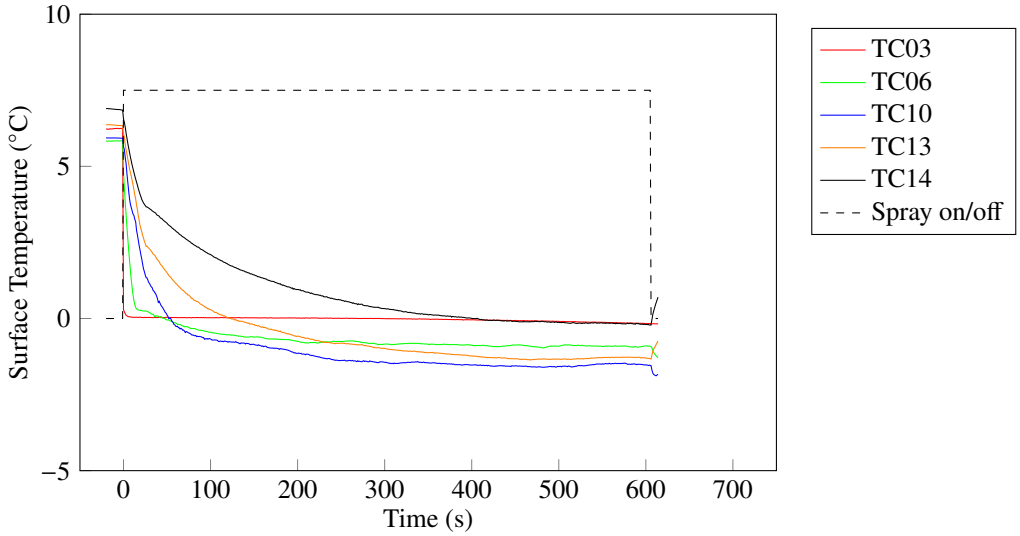

Fig. A.2 Airfoil Surface Temperatures Over Time during Test Condition B.a.

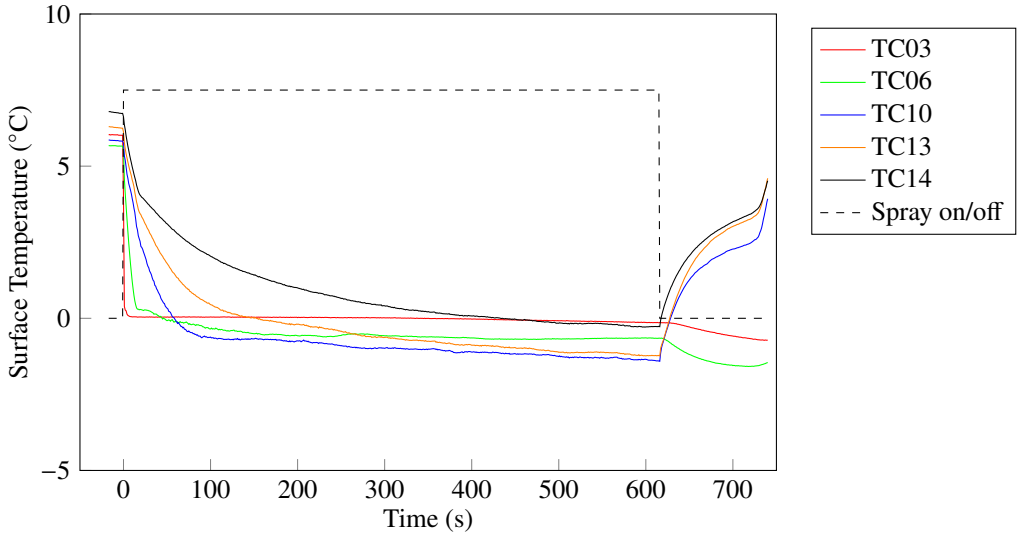

Fig. A.3 Airfoil Surface Temperatures Over Time during Test Condition B.b.

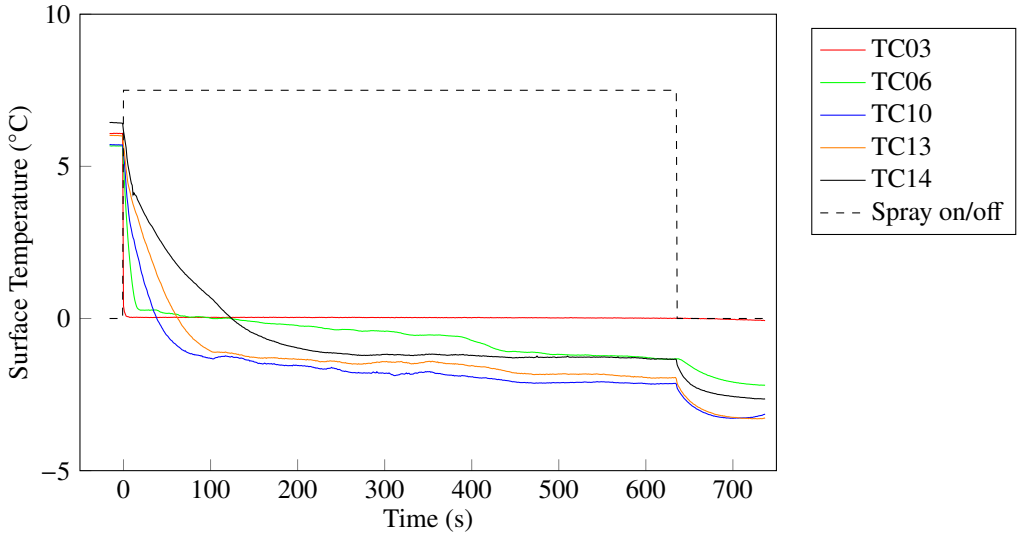

Fig. A.4 Airfoil Surface Temperatures Over Time during Test Condition C.

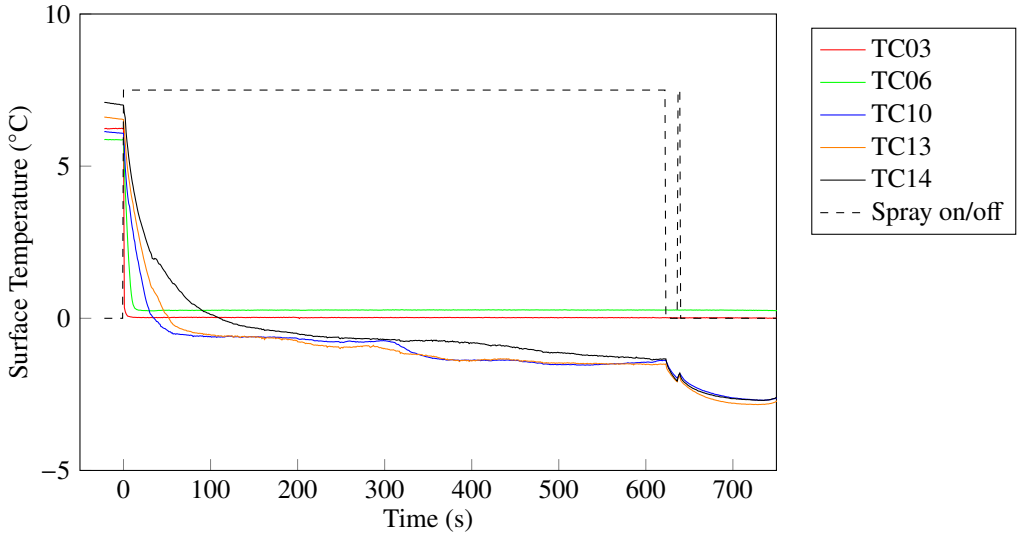

Fig. A.5 Airfoil Surface Temperatures Over Time during Test Condition D.

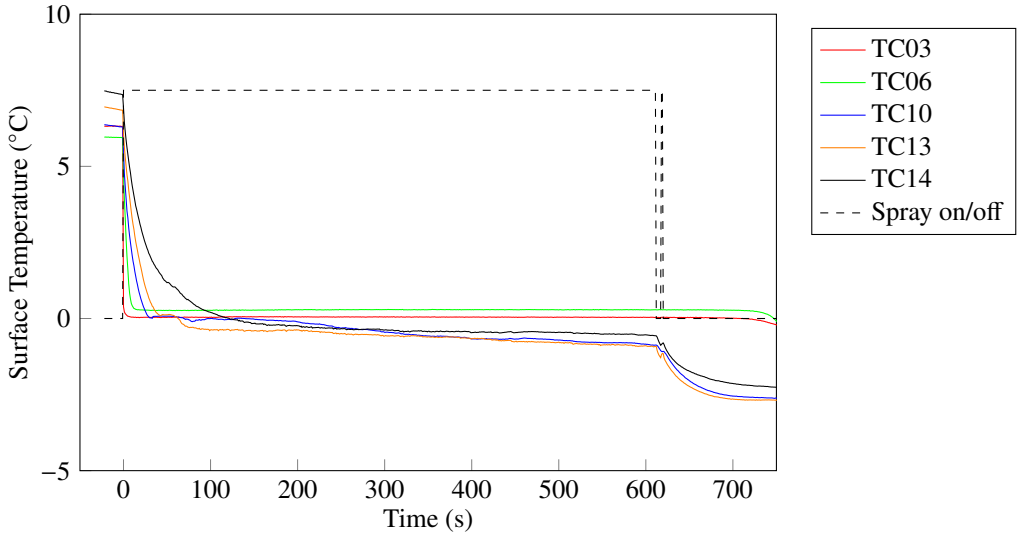

Fig. A.6 Airfoil Surface Temperatures Over Time during Test Condition E.

Acknowledgments

The authors wish to acknowledge the financial support for this work by the Advanced Aircraft Icing (AAI) sub-project of the NASA Advanced Air Transport Technology Project (AATT) under NASA's Advanced Air Vehicles Program. The authors wish to acknowledge the hard work of Michael King in acquiring the particle measurement data during the test campaign. In addition, the authors would like to acknowledge the exceptional support of the PSL staff and NASA Cloud Calibration Team. Finally, the authors would also like to acknowledge the assistance of Dr. Will Bachalo, Dr. Reza Karami, and Dr. Julien Manin of Artium Technologies Inc. for processing the PDI and HSI data.

References

[1] Mason, J., Strapp, W., and Chow, P., "The Ice Particle Threat to Engines in Flight," *44th AIAA Aerospace Sciences Meeting and Exhibit*, American Institute of Aeronautics and Astronautics, Reston, Virigina, 2006. https://doi.org/10.2514/6.2006-206, URL

http://arc.aiaa.org/doi/10.2514/6.2006-206.

[2] Currie, T., Struk, P., Tsao, J.-C., Fuleki, D., and Knezevici, D., "Fundamental Study of Mixed-Phase Icing with Application to Ice Crystal Accretion in Aircraft Jet Engines," *4th AIAA Atmospheric and Space Environments Conference*, American Institute of Aeronautics and Astronautics, Reston, Virigina, 2012. https://doi.org/10.2514/6.2012-3035, URL https://arc.aiaa.org/doi/10.2514/6.2012-3035.

[3] Currie, T. C., Fuleki, D., Knezevici, D. C., and MaCleod, J. D., "Altitude Scaling of Ice Crystal Accretion," *5th AIAA Atmospheric and Space Environments Conference*, American Institute of Aeronautics and Astronautics, Reston, Virginia, 2013. https://doi.org/10.2514/6.2013-2677, URL https://arc.aiaa.org/doi/10.2514/6.2013-2677.

[4] Struk, P., Currie, T., Wright, W. B., Knezevici, D. C., Fuleki, D., Broeren, A., Vargas, M., and Tsao, J.-C., "Fundamental Ice Crystal Accretion Physics Studies," *SAE Technical Papers*, 2011. https://doi.org/10.4271/2011-38-0018, URL https://www.sae.org/content/2011-38-0018/.

[5] Currie, T. C., Fuleki, D., and Mahallati, A., "Experimental Studies of Mixed-Phase Sticking Efficiency for Ice Crystal Accretion in Jet Engines," *6th AIAA Atmospheric and Space Environments Conference*, American Institute of Aeronautics and Astronautics, Reston, Virginia, 2014. https://doi.org/10.2514/6.2014-3049, URL http://arc.aiaa.org/doi/10.2514/6.2014-3049.

[6] Baumert, A., Bansmer, S., Trontin, P., and Villedieu, P., "Experimental and numerical investigations on aircraft icing at mixed phase conditions," *International Journal of Heat and Mass Transfer*, Vol. 123, 2018, pp. 957–978. https://doi.org/10.1016/j.ijheatmasstransfer.2018.02.008, URL https://linkinghub.elsevier.com/retrieve/pii/S0017931017332684.

[7] Trontin, P., Blanchard, G., Kontogiannis, A., and Villedieu, P., "Description and assessment of the new ONERA 2D icing suite IGLOO2D," *9th AIAA Atmospheric and Space Environments Conference*, American Institute of Aeronautics and Astronautics, Reston, Virginia, 2017. https://doi.org/10.2514/6.2017-3417, URL https://arc.aiaa.org/doi/10.2514/6.2017-3417.

[8] Tsao, J.-C., Struk, P. M., and Oliver, M. J., "Possible Mechanisms for Turbofan Engine Ice Crystal Icing at High Altitude," *6th AIAA Atmospheric and Space Environments Conference*, Vol. 51, American Institute of Aeronautics and Astronautics, Reston, Virginia, 2014. https://doi.org/10.2514/6.2014-3044, URL http://arc.aiaa.org/doi/10.2514/6.2014-3044.

[9] Struk, P. M., Bartkus, T. P., Bencic, T. J., King, M. C., Ratvasky, T. P., Van Zante, J. F., and Tsao, J. C., "An initial study of the fundamentals of ice crystal icing physics in the NASA propulsion systems laboratory," *9th AIAA Atmospheric and Space Environments Conference, 2017*, , No. June, 2017, pp. 1–40. https://doi.org/10.2514/6.2017-4242.

[10] Agui, J. H., Struk, P. M., and Bartkus, T. P., "Total Temperature Measurements Using a Rearward Facing Probe in Supercool Liquid Droplet and Ice Crystal Clouds," *2018 Atmospheric and Space Environments Conference*, American Institute of Aeronautics and Astronautics, Reston, Virginia, 2018. https://doi.org/10.2514/6.2018-3970, URL https://arc.aiaa.org/doi/10.2514/6.2018-3970.

[11] King, M. C., Van Zante, J. F., Struk, P. M., Manin, J., and Timko, E. N., "Particle size calibration testing in the nasa propulsion systems laboratory," *2018 Atmospheric and Space Environments Conference*, 2018, pp. 1–13. https://doi.org/10.2514/6.2018-3971.

[12] Struk, P. M., Agui, J., Ratvasky, T., King, M., Bartkus, T., and Tsao, J. C., "Ice-Crystal Icing Accretion Studies at the NASA Propulsion Systems Laboratory," *SAE Technical Papers*, Vol. 2019-June, No. June, 2019, pp. 1–12. https://doi.org/10.4271/2019-01-1921.

[13] Bartkus, T. P., Tsao, J. C., and Struk, P. M., "Analysis of Experimental Ice Accretion Data and Assessment of a Thermodynamic Model during Ice Crystal Icing," *SAE Technical Papers*, Vol. 2019-June, No. June, 2019. https://doi.org/10.4271/2019-01-2016.

[14] Agui, J. H., Struk, P., and Bartkus, T., "Total Temperature Measurements in Icing Cloud Flows Using a Rearward Facing Probe," *SAE Technical Papers*, 2019. https://doi.org/10.4271/2019-01-1923, URL https://www.sae.org/content/2019-01-1923/.

[15] Bartkus, T. P., Struk, P. M., and Tsao, J. C., "Evaluation of a thermodynamic ice crystal icing model using experimental ice accretion data," *2018 Atmospheric and Space Environments Conference*, 2018, pp. 1–18. https://doi.org/10.2514/6.2018-4129.

[16] Agui, J. H., von Hardenberg, P., Chen, R. C., Struk, P. M., and Bartkus, T., "Cloud Uniformity Measurement from NASA's 2nd Fundamental Ice Crystal Icing Test Part 2 (Temperature and humidity)," *AIAA Aviation 2020 Forum*, 2020. https://doi.org/10.2514/6.2020-2840.

[17] Chen, R.-C., Struk, P. M., and Ratvasky, T. P., "Cloud Uniformity Measurement from NASA's 2nd Fundamental Ice Crystal Icing Test Part 1 (Water Content and PSD)," *AIAA AVIATION 2020 FORUM*, American Institute of Aeronautics and Astronautics, Reston, Virginia, 2020. https://doi.org/10.2514/6.2020-2840, URL https://arc.aiaa.org/doi/10.2514/6.2020-2840.

[18] Davison, C. R., Walter Strapp, J., Lilie, L., Ratvasky, T. P., and Dumont, C., "Isokinetic TWC evaporator probe: Calculations and systemic uncertainty analysis," *8th AIAA Atmospheric and Space Environments Conference*, , No. June, 2016, pp. 1–19. https://doi.org/10.2514/6.2016-4060.

[19] Strapp, J. W., Lilie, L. E., Ratvasky, T. P., Davison, C. R., and Dumont, C., "Isokinetic TWC Evaporator Probe: Development of the IKP2 and Performance Testing for the HAIC-HIWC Darwin 2014 and Cayenne Field Campaigns," *8th AIAA Atmospheric and Space Environments Conference*, American Institute of Aeronautics and Astronautics, Reston, Virginia, 2016, pp. 1–28. https://doi.org/10.2514/6.2016-4059, URL http://arc.aiaa.org/doi/10.2514/6.2016-4059.

[20] Struk, P. M., King, M. C., Bartkus, T. P., Tsao, J.-C., Fuleki, D., Neuteboom, M., and Chalmers, J., "Ice Crystal Icing Physics Study using a NACA 0012 Airfoil at the National Research Council of Canada's Research Altitude Test Facility," *2018 Atmospheric and Space Environments Conference*, American Institute of Aeronautics and Astronautics, Reston, Virginia, 2018. https://doi.org/10.2514/6.2018-4224, URL https://arc.aiaa.org/doi/10.2514/6.2018-4224.

[21] Wright, W. B., "User's Manual for LEWICE 3.2," , No. NACA CR-2008-214255, 2008.

[22] King, M. C., Bachalo, W., and Kurek, A., "Particle size measurements from the first fundamentals of ice crystal icing physics test in the NASA propulsion systems laboratory," *9th AIAA Atmospheric and Space Environments Conference, 2017*, , No. June, 2017, pp. 1–21. https://doi.org/10.2514/6.2017-4244.